Nature of Bilayer Lipids Affects Membranes Deformation and Pore Resealing During

Nanoparticle Penetration

Yousef Nademi,[a] Tian Tang,[b] and Hasan Uludağ [a, c, d]

[a] Department of Chemical and Materials Engineering,

[b] Department of Mechanical Engineering,

[c] Department of Biomedical Engineering, and

[d] Faculty of Pharmacy and Pharmaceutical Sciences, University of Alberta, Edmonton, Canada

Abstract

Interactions of nanoparticles (NPs) with lipid membranes have enormous biological implications especially for gene delivery applications. In this work, using all-atom steered- and molecular dynamics simulations, we investigated deformation of lipid membranes and pore closure during a NP penetration process. Three membrane bilayer models built from 2-oleoyl-1-palmitoyl-sn-glycero-3-phosphocholine (POPC), dipalmitoylphosphatidylcholine (DPPC) and dilauroylphosphatidylcholine (DLPC), and a NP formed by 2 short interfering RNA (siRNA) and 6 polyethylenimine (PEI) molecules were used. Our results showed that different membrane lipids could lead to differences in pore formation (symmetric vs. asymmetric), and could undergo different levels of pore-mediated flip-flops during the closure. DLPC showed the largest number of flip-flops among the three lipid membranes. In addition, introduction of hydrophobic linoleic acid (LA) substitution onto the PEIs was found to facilitate pore formation, since the long LA tails could insert themselves into the hydrophobic region of the membrane where the lipid tails were less aligned. Compared with DPPC, POPC and DLPC membranes had less alignment of lipid tails in the bilayer, which promoted the insertion of LA tails and hence NP entry into the cell. Our observations provide valuable insight into the membrane deformations and pore dynamics during NP penetration and will be important for the design of NP carriers for effective gene delivery.

INTRODUCTION

Delivery of genetic material, either deoxyribonucleic acid (DNA) or ribonucleic acid (RNA), into cells has proven to be an effective strategy in treating genetic disorders and cancers [1]. For effective therapy, genetic materials need a carrier to protect them against nucleases and facilitate their cellular entry. In this context, non-viral carriers acquired substantial attention due to their easy-to-engineer and relatively safe nature in comparison to their viral compartments [2]. Among non-viral carriers, the synthetic cationic polymer polyethylenimine (PEI) has received special attention due to the possibility of being easily modified with various functional groups. Its gene delivery performance has been tested extensively in a number of cell models [3]. PEI based nanoparticles (NPs) must enter the cells through a process that involves interaction with cell membrane molecules, where the NPs are expected to preserve their integrity while delivering their cargo into the cytoplasm [4]. Cytoplasmic membranes are vital components of every cell, which may contain hundreds of different lipids distributed between the two bilayer leaflets and crowded with proteins covering ~30% of membrane area [5]. The types of lipids and their spatial configurations define the biophysical properties of the membrane [6]. As an example, the length and degree of saturation of lipid acyl chains govern the thickness and ordering of the hydrophobic region of membranes [6]. Presence of double bonds in the fatty acyl chains of lipids can cause bending of the hydrocarbon chains, thereby affecting the structural and dynamical properties of the membrane[7].

There has been considerable interest in simulative and experimental studies to reveal interaction of NPs with membranes [8–10], especially to understand pore formation and resealing during NP penetration. Membrane pores can be intentionally induced for therapeutic applications, to momentarily enhance membrane permeability and allow therapeutic agents to diffuse into cells [11]. Presence of defects or pores across membranes could lead to unregulated ionic flux and facilitate passive transport of polar molecules [12]. Also, pores can act as initiation sites for structural defects associated with phase transitions, cell fusion, and lysis [12]. *Kwolek et al.*[13], using experiments and molecular dynamics (MD) simulations, studied the role of free PEI molecules on membrane deformation. They found that the electrostatic interactions and hydrogen bonding between PEI and anionic membrane of 2-oleoyl-1-palmitoyl-sn-glycero-3-

phosphocholine (POPC)/1,2-dioleoyl-sn-glycero-3-phosphoric acid (DOPA) induced reorganization of the bilayer in the vicinity of the polymers. This caused pulling of lipid head groups toward the membrane center and the formation of a pore within the membrane structure. *Zhang et al.* [14] using sum frequency generation (SFG) vibrational spectroscopy and attenuated total internal reflection Fourier Transform Infrared Spectroscopy (ATR-FTIR), observed that both linear PEI (lPEI) and branched PEI (bPEI) induced lipid translocations, also known as lipid "flip-flop", in anionic dipalmitoylphosphatidylglycerol (DPPG) as well as zwitterionic distearoylphosphatidylcholine (DSPC) lipid bilayers. *Awasthi et al*. [15] based on their experiments and MD simulations proposed a molecular mechanism for polycation-induced pore formation in membranes. Changes in the membrane structure was attributed to difference in electrostatic potential between the two leaflets of the membrane, induced by polycations. Membrane pores can also be formed through electroporation as a result of applying external electrical fields. MD simulations of *Tieleman et al.*[16] showed that the external electric field interacted with water dipoles, amplified the probability of creating water defects in the membrane interior, and stabilized the formed defects. Experimental and simulation studies showed that pore formation caused by electroporation was highly dependent on the nature of the membrane, where a stronger electric field was required to induce a pore in more ordered membranes that had a larger number of intermolecular hydrogen bonds [17–20]. As a representative example, *Ziegler et al.*[21] using MD simulations found that the minimal threshold of electric field to induce pore formation varied with lipid properties including the chain length and type of acyl chains (i.e., saturated or unsaturated). Specifically, there was a positive correlation between the minimum electric field required to induce the pore and the membrane's thickness as well as the unsaturation level of its acyl chains. Increase in the number of Cs and unsaturated bonds in the acyl chains amplified the required external electric field. Once a transmembrane pore is formed, its fate may be different depending on its size. Below a critical radius, spontaneous resealing occurs [12] whereas above the threshold the pore might lead to irreversible membrane rupture. This emphasizes the need to investigate not only pore formation, but also pore resealing after external stimuli were removed.

Many studies have investigated different membranes in terms of head groups, acyl chains length, and saturation level of lipid chains. *Hyvonen et al.*[7] using MD simulations studied lipid bilayers of dipalmitoylphosphatidylcholine (DPPC) and its mono-, di-, and tetraunsaturated counterparts in the Sn2 position. They found that presence of double bonds substantially reduced the order parameters of CH bonds. Additionally, the double bonds of tetraunsaturated chains were shown to be located in the region spanning from the head group to the bilayer center. On a similar topic, *Zhuang et al.*[22] studied a number of different membrane lipids, including lipids with various head groups (phosphatidic acid (PA), phosphocholine (PC), phosphoethanolamine (PE), phosphoglycerol (PG), and phosphoserine (PS)). It was found that PS had the highest inter-lipid hydrogen bonds, while PG had the most intra-lipid hydrogen bonds. This caused PS and PG bilayers to have the lowest surface area per lipid and the smallest thickness, respectively. In addition, PS, PE and PA lipids had larger contact clusters (5-8 lipids per cluster) than the PC and PG, a size that characterizes the local packing behavior of lipid head groups.

While these studies provided valuable insights into the effect of lipid molecules on membrane features, and mechanism(s) of pore formation caused by small molecules such as free PEIs, it is evident that further studies are required to provide atomistic insight into more complex systems such as the NP interactions with membranes. Previously, our group performed steered MD (SMD) simulations and investigated the stability and configurational changes of NPs formed by PEI and short interfering RNA (siRNA) during penetration into the zwitterionic POPC membrane [23]. Three types of PEI molecules, namely unmodified PEI and PEIs modified with caprylic (CA) and linoleic acids (LA), were employed. The structural changes in the PEI-LA/siRNA NP were minimal, while the PEI-CA/siRNA NP showed the largest structural changes. In a more recent study [24], we investigated the effect of membrane surface molecules on the integrity and configurational changes of NPs, using a combined simulation and experimental approach. We found that anionic POPS lipids can dissociate the NPs, while zwitterionic POPC lipids did not induce dissociation. Additionally, LA substitution was found to enhance the stability of PEI/siRNA NPs. While those studies were beneficial for the understanding of structural changes in NPs, the effect of NP penetration on the integrity of membranes has not been explored. To the best of our

knowledge, the present work is the first all-atom study that investigated the interplay between PEI NPs and various lipidic membrane models where the acyl chain lengths and saturation levels were altered. SMD and MD simulations were employed for zwitterionic POPC, DPPC, and dilauroylphosphatidylcholine (DLPC) membranes in this study. These membranes have the same surface properties, but possess different acyl chain properties. Native and LA-modified PEIs were adopted as polynucleotide carriers, since LA-modified PEIs have proven to be an exceptionally effective carrier for gene delivery in our experimental studies [25,26]. Our focus in this study was to investigate (*i*) pore formation and resealing mechanism during NP penetration, and (*ii*) the effects of acyl chain features of the membrane lipids, and carrier properties on pore formation.

METHODS

Simulated systems and procedure

Two types of NPs were simulated, each comprised of 2 siRNA molecules and 6 branched PEIs (bPEIs). The model siRNA has the sense strand of 5'- CAGAAAGCUUAGUACCAAATT-3' and antisense strand of 5'-UUUGGUACUAAGCUUUCUGTC-3'. It is used to silence P-glycoprotein [27] and consists of 42 nucleotides with a total charge of −40 in its fully deprotonated state. The chemical structure of simulated PEI is shown in Fig. 1a. The PEI in its native form has a molecular weight of 1874 Da and is composed of 43 amino groups. Twenty of these amino groups were protonated, equivalent to the protonation ratio of 47%, which was in the range of reported protonation ratio (10 to 50% [28–31]) for PEI at physiological pH. For simplicity, the NP formed by 2 siRNAs and 6 native PEIs was referred to as PEI NP (see Table 1). The other simulated NP was denoted as PEI-LA NP in Table 1, where each PEI was modified with 3 hydrophobic substitutions of LA. The chosen substitution level was in line with the practical range of modification used for siRNA delivery [32]. The initial structures of NPs were adopted from our previous study where they were equilibrated at 310K. Then, to equilibrate the NPs at 323K that was above the phase transition temperature of our simulated membrane lipids, each NP was solvated with TIP3P [33] water molecules and ions (150 mM KCL) and subjected to 7 ns (restrained) + 33 ns (free) simulation. The final

equilibrated structure of each NP was adopted as the initial configuration of the NP for SMD simulations of membrane penetration (see Supporting Information (SI), Figs. S1 and S2).

Three membrane lipids, POPC, DPPC and DLPC, were used, and their chemical structures are shown in Fig. 1b. Among these lipids, DLPC has the shortest lipid tails (12:0, 12:0), where the first indices represent the number of C atoms in Sn1 and Sn2 chains (12 and 12 here), and the second indices specify the number of unsaturated carbons in each chain (0 and 0 here). The tails of DPPC (16:0, 16:0) and POPC (16:0, 18:1) are of similar length, but differ in terms of saturation, where POPC has one unsaturated carbon on its Sn2 chain. The initial structure of POPC bilayer was adopted from our previous study[23]. DPPC and DLPC bilayers were constructed using Membrane Builder [34] in CHARMM-GUI [35,36]. Similar to the NPs, the membranes were equilibrated by 50 ns MD simulations until the area per lipid reached $60.45 \pm 0.34 \text{ } Å^2$ and $63.21 \pm 0.53 \text{ } Å^2$ (data collected from the last 20 ns), respectively for DPPC and DLPC, which agreed with the values reported in the literature [37,38]. The final equilibrated configurations were adopted as the input structures for SMD simulations with NPs (see SI, Figs S3-S6).

SMD simulations assist in accelerating the penetration process and also mimic the situation where the NPs are pulled by external or biological forces towards the interior of the cell membrane. In each SMD the system was prepared by first placing the NP above the membrane so that the center of mass (COM) distance between the NP and the membrane was 8 nm. Initial orientation of the NP was chosen in a way such that the axes of its siRNAs were almost perpendicular to the membrane surface, while the effect of initial orientation was explored via replica simulations described later. Then, upon solvation with TIP3P [33] water and 150 mM KCL, the system was equilibrated for 6 ns with a harmonic restrain of 10 kcal mol^{-1} Å^{-2} exerted on the non-H atoms of the NP. The equilibrated membrane-NP system was used next for the SMD simulation, where the COM of the NP was attached to a dummy atom via a virtual spring and the spring was pulled with a constant velocity along the z direction perpendicular to the membrane surface. The pulling speed $v = 5$ Å ns^{-1} and spring constant $k = 5$ kcal mol^{-1} Å^{-2} were used. In the literature, pulling speeds in the range of 0.1 to 100 Å ns^{-1} have been reported for SMD simulations, while lower values of pulling speed have been used to determine the potential of mean force [39–45]. Previously[23], we explored

the effect of pulling speed and showed that $v = 5$ Å ns^{-1} was suitable for studying membrane penetration of NPs. Each SMD simulation took 34 ns for the NP to travel a total distance of 170 Å. In Table 1, PEI NP-POPC, PEI NP-DPPC and PEI NP-DLPC are respectively the SMD simulations for the PEI NP crossing POPC, DPPC and DLPC bilayers. The corresponding SMD simulations for the PEI-LA NP are PEI-LA NP-POPC, PEI-LA NP-DPPC and PEI-LA NP-DLPC. One replica simulation was performed for each system involving the PEI-LA NP, where the axes of its siRNAs were almost parallel to the membrane surface in the initial configuration. The replica systems were named PEI-LA NP-replica-POPC, PEI-LA NP-replica-DPPC and PEI-LA NP-replica-DLPC.

At last, the final configurations from the SMD simulation were used to investigate pore closure by MD simulations without restraints. Specifically, the NP in each system was removed and the deformed membrane was solvated again with TIP3P[33] water and 150 mM KCL. Each of the nine membrane systems was then subjected to 64 ns MD. These systems are labeled in Table 1 as POPC (PEI NP), DPPC (PEI NP), DLPC (PEI NP), POPC (PEI-LA NP), DPPC (PEI-LA NP), DLPC (PEI-LA NP), POPC (PEI-LA NP-replica), DPPC (PEI-LA NP-replica) and DLPC (PEI-LA NP-replica).
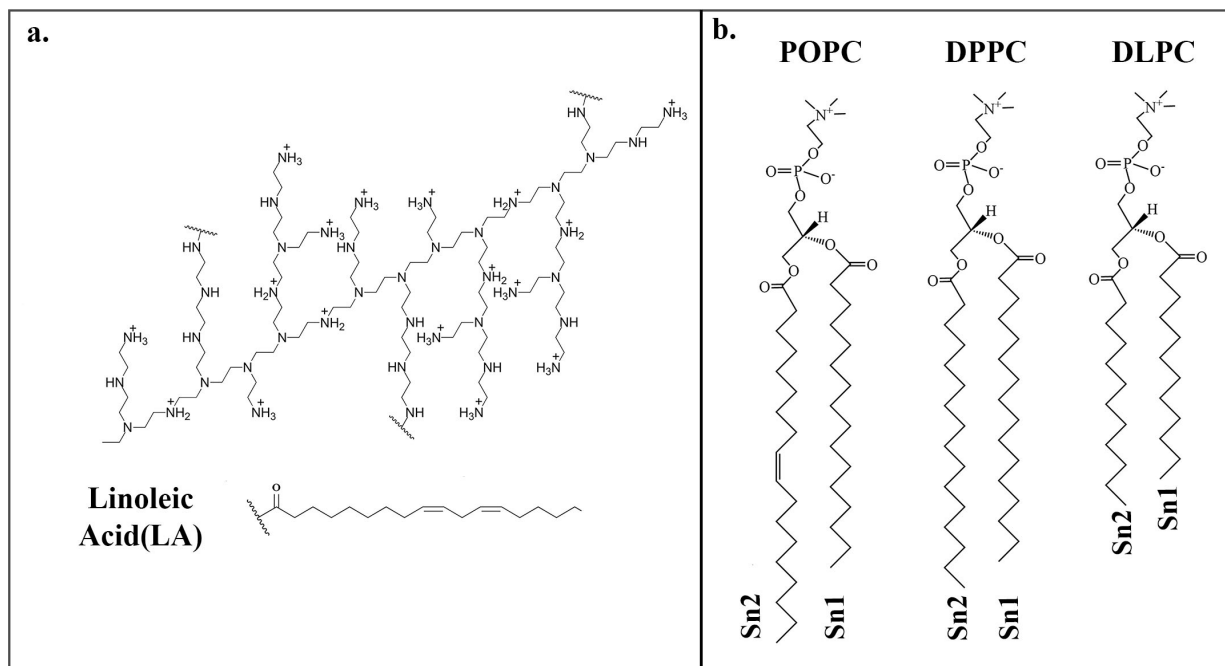

Figure 1. (a) Molecular structure, protonation sites and lipid substitution sites of the simulated PEIs, (b) structures of POPC, DPPC, and DLPC molecules.

Table 1. Detailed information of the simulated systems in this study.

System	No. atoms	Simulation box size ($Å^3$)	Lipid on each PEI	PEI/siRNA charge ratio	Simulation time (ns)
PEI NP	85640	90×100×100	None	1.5	40
PEI-LA NP	93691	100×90×100	3 LA	1.27	40
PEI NP-POPC	990451	160 ×180×340	None	1.5	34
PEI NP-DPPC	1018962	160×200×340	None	1.5	34
PEI NP-DLPC	1015417	180×170×340	None	1.5	34
POPC (PEI NP)	658088	160×180×230	None	-	64
DPPC (PEI NP)	632815	160×200×320	None	-	64
DLPC (PEI NP)	633654	180×170×220	None	-	64
PEI-LA NP-POPC	990473	160 ×180×340	3 LA	1.27	34
PEI-LA NP-DPPC	1019002	160×200×340	3 LA	1.27	34
PEI-LA NP-DLPC	1015459	180×170×340	3 LA	1.27	34
POPC (PEI-LA NP)	572647	160×180×200	3 LA	1.27	64
DPPC (PEI-LA NP)	606802	160×200×310	3 LA	1.27	64
DLPC (PEI-LA NP)	605079	180×170×220	3 LA	1.27	64
PEI-LA NP-replica-POPC	990473	160 ×180×340	3 LA	1.27	34
PEI-LA NP-replica-DPPC	1019002	160×200×340	3 LA	1.27	34
PEI-LA NP-replica-DLPC	1015459	180×170×340	3 LA	1.27	34
POPC (PEI-LA NP-replica)	572647	160×180×200	3 LA	1.27	64
DPPC (PEI-LA NP-replica)	606802	160×200×310	3 LA	1.27	64
DLPC (PEI-LA NP-replica)	605079	180×170×220	3 LA	1.27	64

Simulation details

Force field parameters for the PEI molecules were adopted from a previous study [46] by our group, which were generated according to CHARMM General Force Field and validated with *ab initio* calculations. A CHARMM 36 [47,48] Force Field was used for other molecules. All simulations were performed using NAMD [49] molecular dynamic package and in NPT ensemble. Time steps of 2 fs and periodic boundary conditions (PBC) were applied. Particle Mesh Ewald [50] (PME) method was employed to calculate long-ranged electrostatic interactions. The cut off distance was set to 12 Å for van der Waals and short-range electrostatic interactions. The SHAKE [51] algorithm was used for constraining bonds involving H atoms. To maintain the temperature (323K), Langevin dynamics thermostat was used. The pressure was maintained using a semi-isotropic pressure control that decouples the direction normal to the bilayer and the plane of the bilayer. Nose-Hoover Langevin barostat was applied to achieve 1 bar pressure, with a damping time

scale of 100 fs and a Langevin piston oscillation period of 200 fs [52,53]. For visualization and analysis of simulation trajectories, VMD [54] was used.

RESULTS

Membrane deformations during penetration of PEI NP

Penetration of the PEI NP induced membrane deformation during its entry. To measure the deformation, the positions of all P atoms are shown in Fig. 2 at different timeframes. All membranes experienced a disruption in their integrity as the NP penetrated. At 10 ns, the disturbance started first in the upper leaflet while the lower leaflet maintained its integrity. At 20 ns, the membranes bent and both leaflets underwent deformation. At 34 ns, the deformation of the membranes was severe, and the P atoms no longer maintained a continuous network as in the earlier timeframes, suggesting the formation of a pore in each membrane. The disruption of the upper leaflet was larger than the lower leaflet, evidenced by the more significant deviation of the P atoms from their initial positions in the upper leaflet. While all membranes showed a similar trend, the level of disruption varied for different membranes. At 34 ns, the P atoms in the POPC bilayer could be found further from their initial positions compared with DPPC and DLPC bilayers, indicating more severe disintegration of the POPC membrane. DLPC displayed lower deviation of the P atoms from their initial positions than the other two membranes, which can be attributed to its lower resistance against pore formation due to its smaller thickness (Fig. S4) and weaker hydrophobic-hydrophobic interactions among its lipid tails.
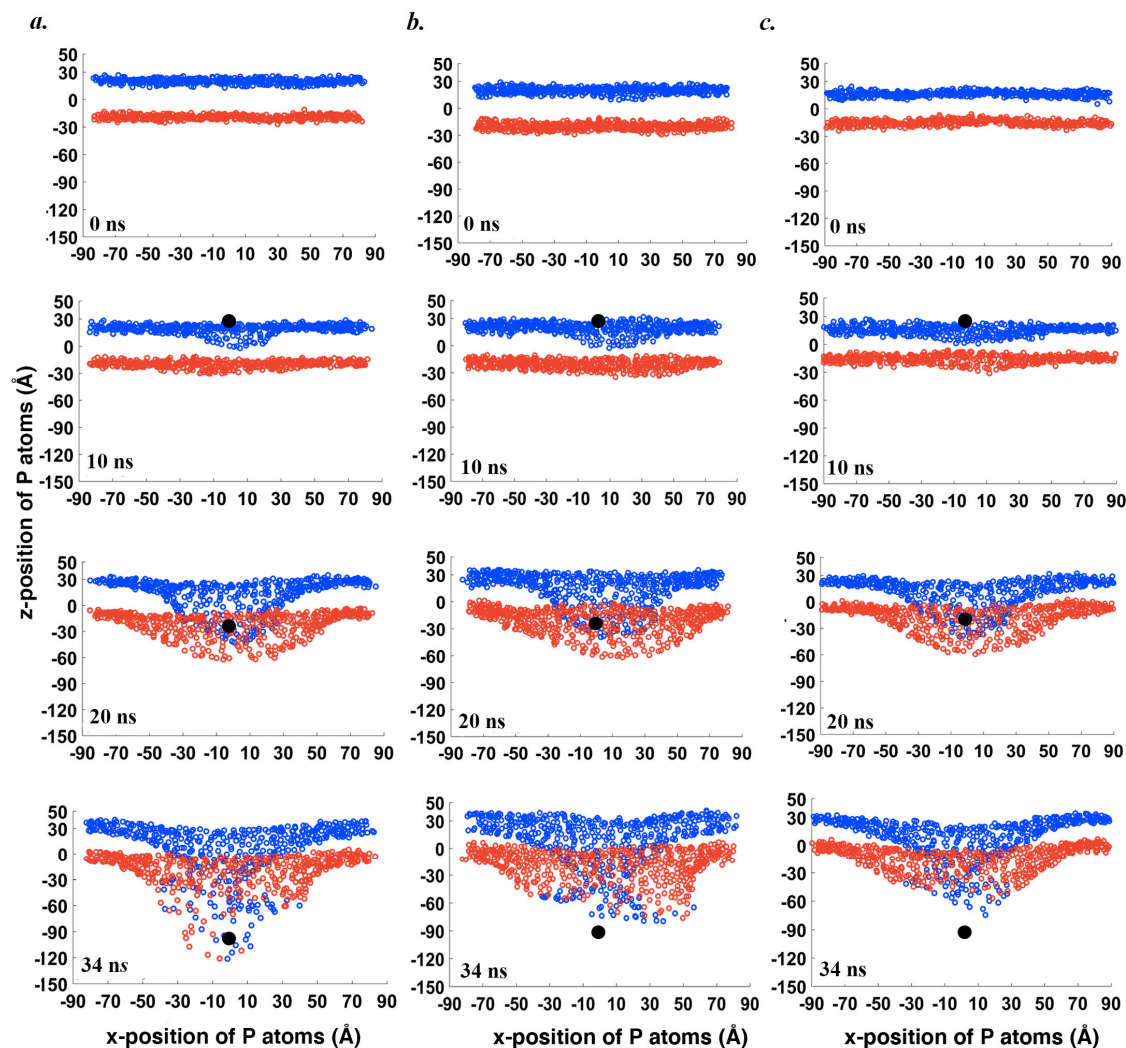
Figure 2. Positions of P atoms in the (blue) upper and (red) lower leaflets of (a) POPC (b) DPPC and (c) DLPC membranes during penetration of the PEI NP. The black circle represents COM position of NP.

Pore formation caused by PEI NP penetration

Penetration of the PEI NP induced a pore within each membrane. To quantify the size of the formed pore under the pulling force, the positions of P atoms were first projected onto the x-y plane which was parallel to the membrane surface. The same projection was done for the COM of the PEI NP. Then the in-plane distribution of the P atoms around the COM, in terms of areal density (number of P atoms per unit area), was calculated and shown in Fig. 4 (see SI, Fig. S7 for calculation details). For each membrane, Fig. 3 shows the distribution at three stages: when the membrane was initially undisturbed, when the pore was

well established, and at the end of the pulling process in SMD. It is worth noting that the time for a well-established pore, determined from visual observation of the pore transitioning from increasing to decreasing trends, was different for each membrane: 30, 27, and 24 ns, respectively for POPC, DPPC, and DLPC membranes. For undisturbed membranes (blue curves), as the distance from the COM of NP increased, the distribution remained relatively constant. When the pores were well established (red curves), the distribution was zero near the COM of the NP while showing two peaks at larger distances. The first peak (location denoted by r_1) corresponded to the edge of the formed pore where the lipids accumulated, representative of the pore size. The second peak (location denoted by r_2) corresponded to the region where membrane was significantly bent downwards so that the projection of the P atoms onto the x-y plane showed a high local areal density. r_1 was found to be ∼26, ∼30 and ∼33 Å for POPC, DPPC and DLPC membranes, respectively. This shows that the pore size was largest for the DLPC membrane, which agrees with experimental studies where pore formation was found easier in lipidic membranes with shorter hydrocarbon tails [55]. Values of r_2 were ∼52, ∼57 and ∼58 Å for POPC, DPPC and DLPC, respectively. The largest r_2 for DLPC was consistent with its largest pore size, i.e. r_1, among the three membranes. Compared with DPPC, POPC showed smaller values for both r_1 and r_2, while the difference in r_2 was more significant. Consulting Fig. 2, POPC underwent more significant bending deformation during pore formation, which allowed membrane rupture to occur at a shorter distance from the NP. In contrast, DPPC experienced a more gradual deformation that was less localized than POPC and covered a larger area of the membrane. At the end of the pulling process (green curves), the first peak underwent a decrease in height and a shift to the left for the POPC and DPPC membranes, and the changes were more profound for the latter. For the DLPC membrane, the first peak disappeared completely. In addition, the height of the second peak showed a decrease for POPC and DLPC membranes. This suggests that within our simulation time (34 ns), resealing of the pore started almost immediately after the NP began to detach from the membrane. The recovery was highest for the DLPC membrane and lowest for POPC. Although DLPC had the largest pore size, as can be seen from Fig. 2 its deformation was the least among the three membranes. The thinnest bilayer provided the least resistance to NP entry, and a large pore was able to form without creating significant displacement

12

of the lipids. Consequently, the less lipid displacement facilitated recovery during pore resealing. The opposite is true for POPC, which exhibited the most severe disintegration and largest lipid displacement that are hardest to recover.
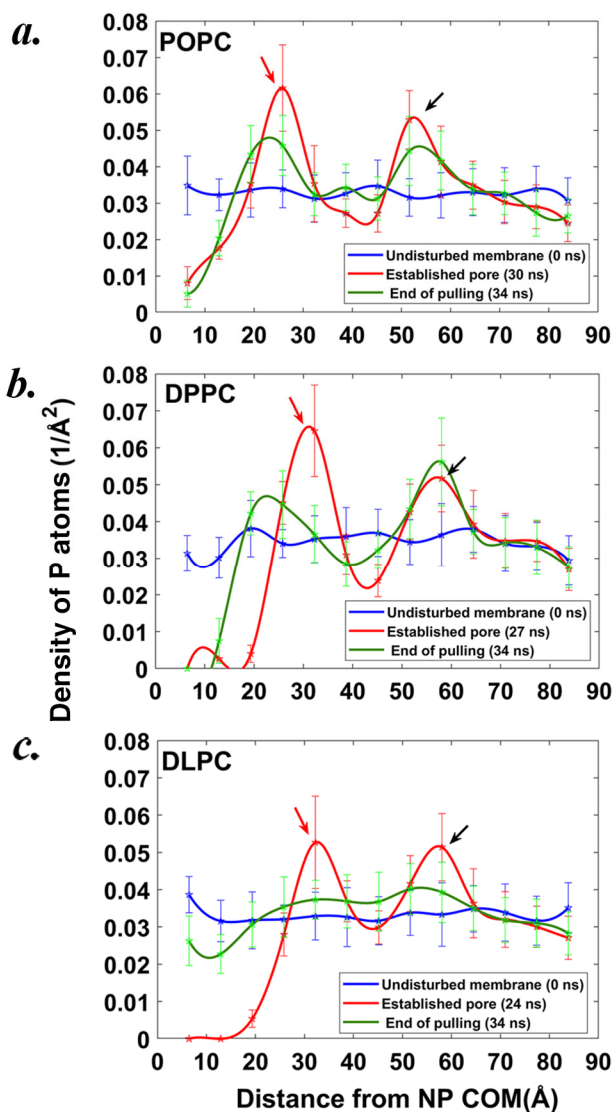

Figure 3. Distribution of P atoms around the COM of PEI NP, within the x-y plane, for (a) POPC, (b) DPPC, and (c) DLPC membranes (see SI Fig. S7 for calculation details). Red and black arrows in each subfigure point to the locations of the first and second peaks respectively, for the established pore.

Along with the difference in pore size, the three membranes also showed difference in the order and orientation of the acyl chains. To quantify the order in the lipid tails under non-equilibrium pulling of the NP, the probability distribution (PD) of the angle formed between Sn1 and Sn2 acyl chains was

monitored. To this end, an angle (θ) was defined between two vectors each associated with one acyl chain (see Fig. S8 for details). $\theta = 0°$ corresponds to parallel orientation between Sn1 and Sn2 chains, whereas $\theta = 90°$ represents perpendicular orientation between them. Fig. 4 shows the PD of θ at 0, 20, and 34 ns. For all membranes, as time increased and NP penetration progressed, the PD became wider and there was a decline in the peak value, suggesting a reduction in the order of the membrane. At 0 ns, the most probable angle between the two lipid tails was respectively ~27°, ~22° and ~28° for POPC, DPPC and DLPC membranes. POPC and DLPC had a wider PD than DPPC, indicating that POPC and DLPC were less aligned and more dynamic. For POPC this originates from the presence of unsaturated Cs on its Sn2 chain which can induce a change in orientation of the chain and cause the POPC membrane to have a lower thickness (as shown in Fig. S4). For DLPC, on the other hand, the short acyl chains are the source of the smaller degree of order. The alignment of DPPC lipids increased the intermolecular interaction among them, causing the membrane to be more rigid. Also, the larger angle between two lipid tails in POPC and DLPC has led to a slightly higher free volume within the bilayers than in the DPPC membrane (See SI, section S5), which may impact the configurational changes of the NP during its entry.
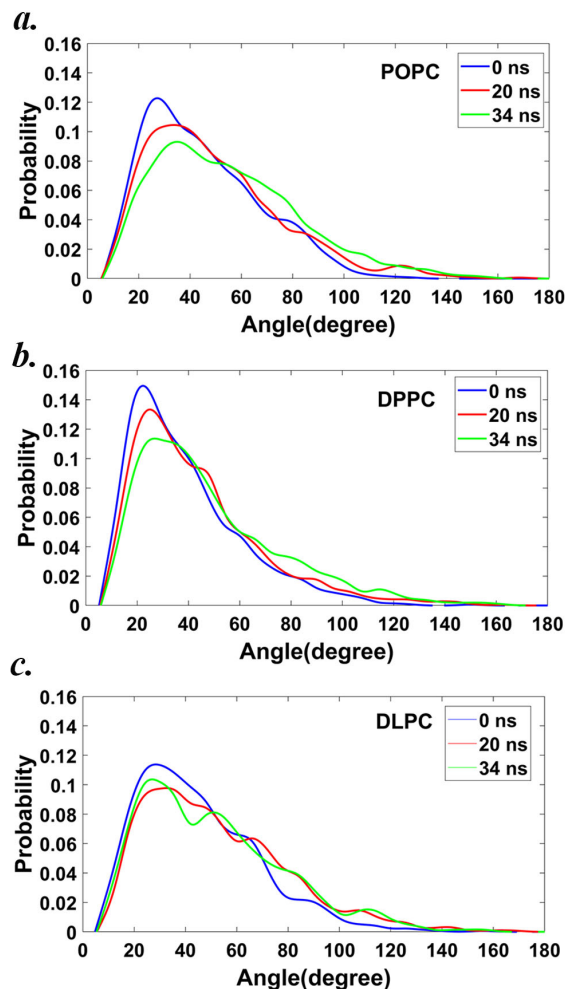
Figure 4. Probability distribution of the angle between Sn1 and Sn2 chains for (a) POPC, (b) DPPC and (c) DLPC membranes.

Interaction between membrane and PEI NP

To evaluate the interplay between PEI NP and the membranes during the non-equilibrium SMD, pulling force and structural parameters of the NP were monitored. Fig. 5a shows the pulling force on the PEI NP, plotted against the COM position of the NP. Side-view snapshots of the NP and the membrane at different time during the penetration are shown in SI (Fig. S9). All systems followed a similar trend. The force was relatively constant when the NP was approaching the membrane, followed by an increase up to a maximum value. The increase in force originated from the resistance of membrane to deformation and disintegration. Finally, the force decreased as the NP detached from the membrane, although it did not return to the value measured before penetration began because at the end of each simulation some

membrane lipids were still attached to the NP (Fig. S9). Despite these similarities, the force profiles displayed certain quantitative differences. The maximum force was about $2900, 2880$ and 2410 *pN* respectively for POPC, DPPC and DLPC membranes. This indicates that the resistance to the passage of the NP was higher in POPC and DPPC membranes than the DLPC membrane. This is not surprising, as the POPC and DPPC bilayers had larger thickness (Fig. S4) and hence larger bending stiffness. The bending modulus, which is a macroscopic constant that represents the ability of a material to oppose bending [56], was reported to be $25.7 \pm 2.1, 27.5 \pm 3.4$, and 20.4 ± 1 *kT*, respectively for POPC, DPPC and DLPC vesicles [57], where *k* is the Boltzmann constant and *T* is temperature. The bending modulus reported in previous MD simulations [58] was $25.3 \pm 0.6, 34.1 \pm 0.9$, and 25.8 ± 0.6 *kT*, respectively for the POPC, DPPC, and DLPC membranes. The difference from the experimental values might be caused by the different temperature, salt concentration, and number of lipid molecules used in the MD simulations. The force profiles for POPC and DPPC membranes almost overlapped except during detachment of the NP (z-position of COM 50-90 Å), where the force was higher for POPC. Considering that POPC and DPPC have a similar bending modulus, the increase in the force was caused by the higher degree of deformation in POPC membrane during NP detachment of NP as shown in Fig. 2.
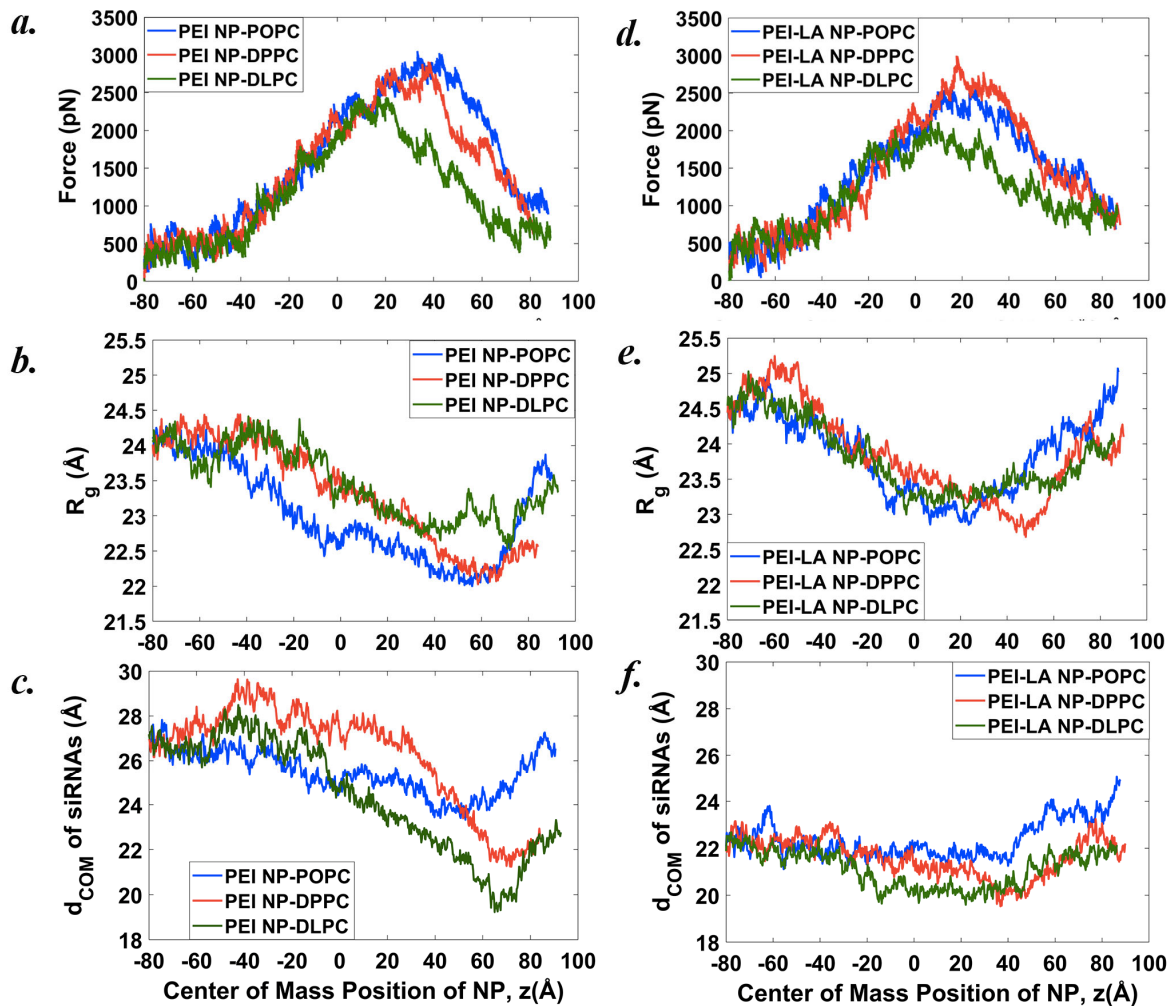
Figure 5. (a,d) Force profile, (b,e) gyration radius and (c,f) d_{COM} distance between the two siRNAs, as functions of COM position of the NP. The left and right graphs are for PEI and PEI-LA NPs, respectively.

The smaller degree of alignment, i.e. order, of POPC and DLPC lipids is expected to affect the NP penetration. Specifically, these two membranes provide a slightly higher free volume within the bilayers for possible configurational changes of the NP as discussed in Fig. 4. To monitor the configurational changes, gyration radius (R_g) of the NP and COM distance between the two siRNAs (d_{COM}) were assessed as a measure of NP compactness (Fig. 5b and 5c). Additionally, the shape anisotropy of the NP, relative orientation of the two siRNAs, and orientation of each siRNAs relative to the z-axis were also measured and discussed (SI, section S7). For all membranes, both R_g and d_{COM} showed an initial decreasing trend,

indicating some degree of compaction for the NP. Since the short siRNAs were relatively rigid, the NP compaction could occur through compaction of the constituent PEIs, and/or reduction in d_{COM}. The relative reduction in R_g was ~8.20%, ~8.21%, and ~5.8%, while the relative reduction in d_{COM} was ~13.1%, ~20.66%, and ~28.78%, respectively for POPC, DPPC and DLPC membranes. This suggests that for POPC, both mechanisms played similar roles in compacting the NP, while for DPPC and DLPC the majority of the compaction was caused by a reduction in d_{COM}. POPC and DPPC have a similar length in their acyl chains, but highly aligned tails of the latter membrane necessitated the larger magnitude of reduction in d_{COM} to minimize membrane disruption. Interestingly, the minimum value of R_g, denoted as $(R_g)_{min}$, showed a positive correlation with the size of the established pore (Fig. 3). $(R_g)_{min}$ was the same for POPC and DPPC, which was lower than $(R_g)_{min}$ for DLPC. Meanwhile, the pore size was largest for DLPC, while being the same for POPC and DPPC. For DLPC where pore formation was easier (Fig. 5a), the size of the established pore was larger, and $(R_g)_{min}$ of NP was larger. After reaching the minimum of R_g and d_{COM}, the NP behaved differently for the three membranes. For POPC, both R_g and d_{COM} displayed full recovery to their original values during NP exit. For DPPC, NP showed little recovery from its compacted configuration. For DLPC, R_g was fully recovered, while d_{COM} showed only partial recovery. The high alignment between the lipids of DPPC (as shown in Fig. 4) caused the NP to retain its compressed configuration, while the less alignment of the Sn1 and Sn2 chains in POPC allowed more space for the NP to relax and recover during membrane crossing.

Membrane recovery and pore closure

Visual examination of the simulation trajectories revealed that depending on the membrane type, two types of pores, namely asymmetric and symmetric, were formed. In the former case (Fig. 6a), one side of the bilayer deformed more and moved along with the NP as it exited; while in the latter case (Fig. 6b), the deformation of the membrane was symmetric around the NP. The overall deformation and disruption of the membrane were therefore larger if the pore was asymmetric. Among the three membranes, POPC (Fig. 6c) exhibited asymmetric pore formation, while DPPC (Fig. 6d) and DLPC (Fig. 6e) showed

symmetric pore formation. A quantitative measure of pore symmetry at the end of pulling process (34 ns) is provided in SI, section S8.
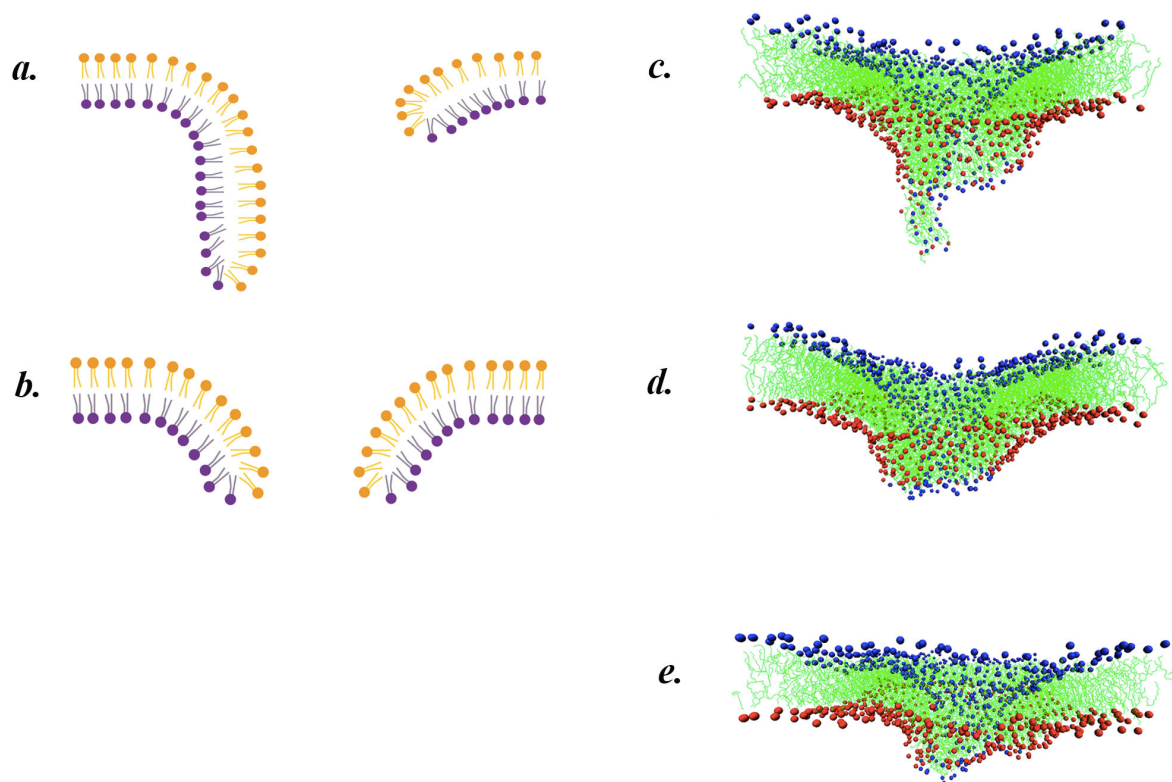

Figure 6. Formation of two types of pores: (a) asymmetric, (b) symmetric, and side-view snapshots at 34 ns for (c) POPC, (d) DPPC and (e) DLPC membranes. P atoms of upper and lower leaflets are shown in blue and red, respectively. The lipid tails are shown in green.

To measure membranes' recovery from its deformed configurations, MD simulations were performed by removing the NP and allowing the pore to close. Fig. 7 shows the position of P atoms at different times. All membranes started recovery towards their undeformed flat configuration immediately after NP removal. However, the degree of recovery was different at the end of the 64 ns of equilibrium MD simulation: both DPPC and DLPC fully regained their flat configuration, while POPC seemed to require more time for a complete recovery. During the recovery, the number density of lipids at the lower leaflet increased for all membranes as lipids from the upper leaflet joined the lower leaflet (blue circles on the

lower leaflet in Fig. 7). This imbalance increased the probability of lipid flip-flops between the leaflets. By 64 ns, lipid translocation from the lower leaflet to the upper leaflet had occurred to a small degree for POPC (3 lipids) and to a higher degree for DLPC (19 lipids), while DPPC displayed no lipid translocation from the lower to the upper leaflets. The high degree of flip-flops in the DLPC membrane originated from its short acyl chain length which allowed the lipids to be more dynamic. The smaller thickness of the DLPC membrane is also expected to pose a lower energy barrier, compared with the other two membranes, for the exchange of lipids between the two leaflets.
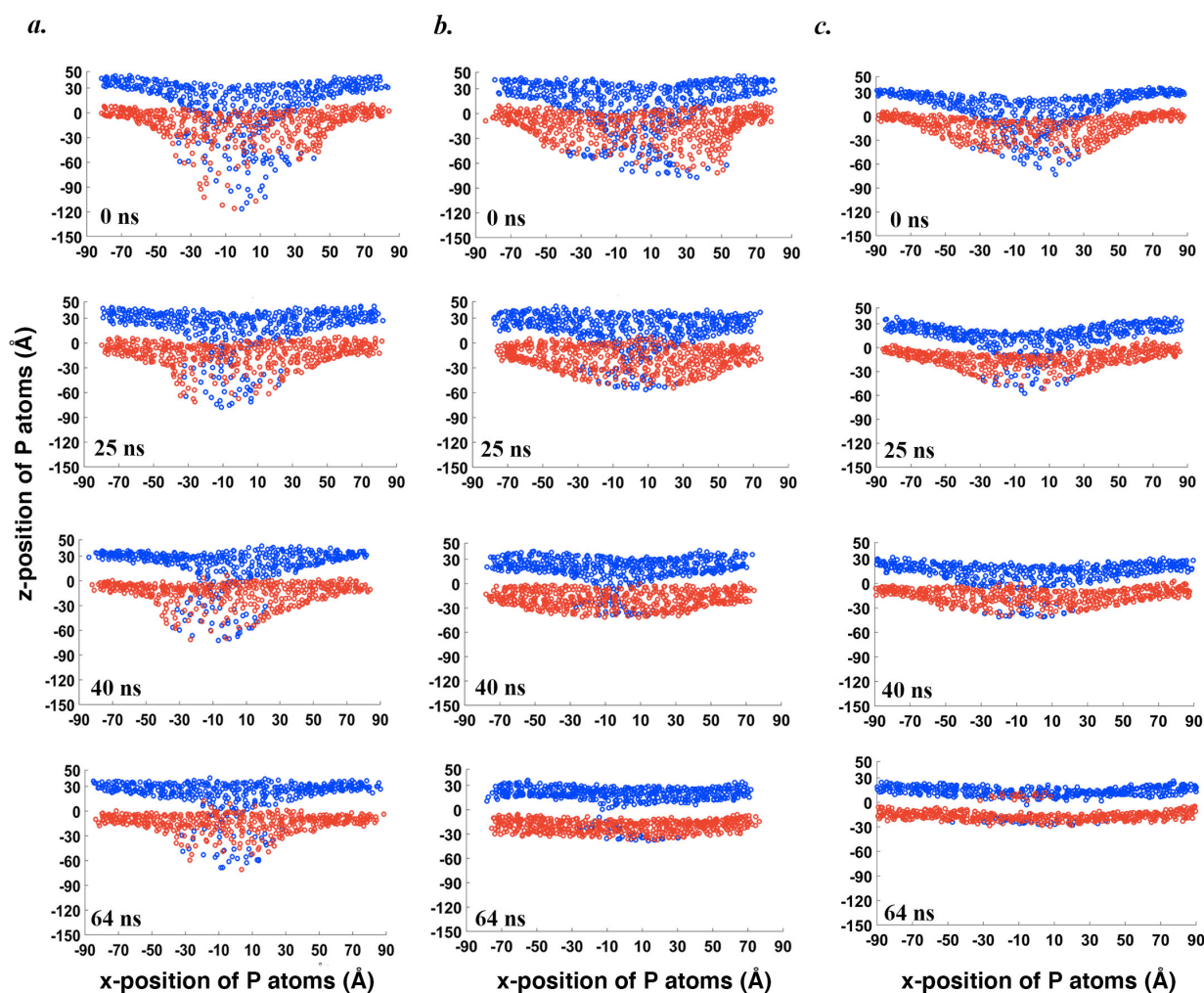

Figure 7. Position of P atoms in the (blue) upper and (red) lower leaflets of (a) POPC (b) DPPC and (c) DLPC membranes during pore recovery.

Depending on the types of the formed pore (symmetric or asymmetric), the process of resealing differed. Fig. 8 shows a simplified schematic of pore resealing process (See SI, section S8 for the information on the representative simulations videos). For an asymmetric pore (Fig. 8a), the lipids in the vicinity of the pore first moved toward each other to reduce their exposure to water. When the pore size was sufficiently reduced and the lipids initially surrounding the pore started making contact, lateral diffusion of the lipids began to reduce the curvature of the membrane. Due to the asymmetric feature of the pore, the lower leaflet on one side of the pore could readily contact the upper leaflet on the other side (see step 2 in Fig. 8a). As such, some lipids from the lower leaflet was able to diffuse into the upper leaflet, leading to flip-flop, which continued until the pore was completely sealed.
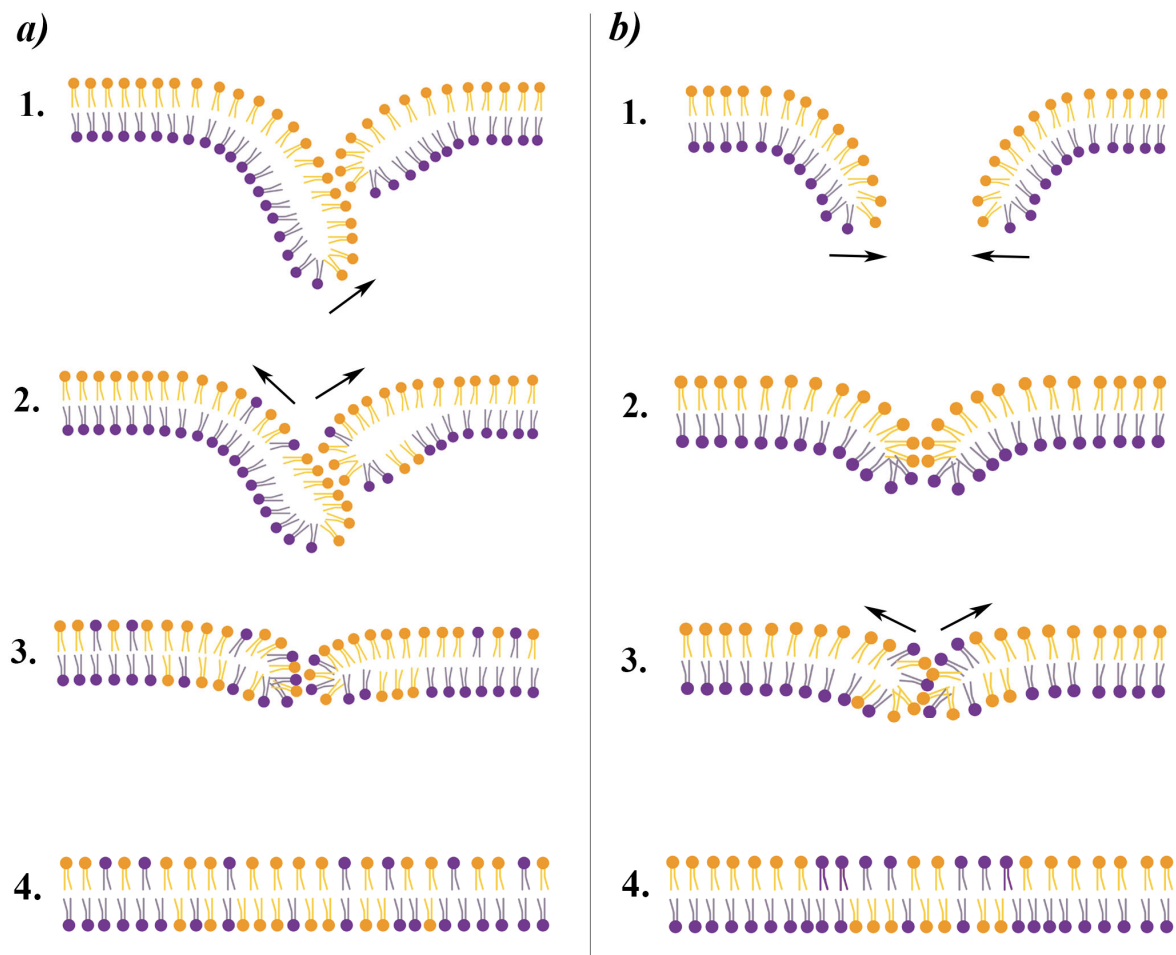

Figure 8. Process of pore resealing for (a) an asymmetric pore, and (b) a symmetric pore.

For the symmetric pore (Fig. 8b), the resealing process was similar at the beginning. However, the symmetric nature of the pore did not facilitate the contact between the lower leaflet of one side with the upper leaflet of the other side. Consequently, the diffusion of the lipids from the lower leaflet to the upper leaflet did not occur until much later in the resealing process (see step 3 in Fig. 8b). In addition, the resealing of a symmetric pore was faster than an asymmetric pore due to the overall smaller disruption of the membrane during the pore formation. For example, in Figure 7 the asymmetric pore in the POPC membrane did not return to its flat configuration at 64 ns of the resealing simulation. On the other hand, the symmetric pores in the DPPC and DLPC membranes were close to being flat at 40 ns, and completed resealed at 64 ns. As a result, the lipids that underwent flip-flop were more concentrated at the pore site rather than migrating further from the pore location. Table S3 in the SI shows that the flip-flops occurred as early as 40 ns in the POPC membrane which contained an asymmetric pore, while flip-flops in the DLPC membrane, with a symmetric pore, did not occur until the end of simulation.

Effect of PEI-LA NP on membranes

The effect of PEI-LA NP penetration on membrane integrity was qualitatively similar to PEI NP, with some slight quantitative differences. Selected results are presented here while others can be found in the SI (Figs. S16-S17). For POPC and DLPC, the force required to pull the PEI-LA NP through the membrane was lower than the PEI NP, while the force was similar for the two NPs in the case of DPPC (Fig. 5d). Fig. 9 shows both the PEI-LA NP and the hydrophobic tails of the membrane during each penetration process (hydrophilic part of the membrane not included for the simplicity of visualization). Examination of the figure shows that the hydrophobic LA substitutions (purple color) were exposed to the interiors of the POPC and DLPC bilayers during the early stages of the process. On the contrary, the LA substitutions conformed well to the NP and did not insert themselves into the DPPC bilayer until the very end. The interaction of LA substitutions with the hydrophobic part of the lipid bilayer facilitated NP entry and reduced the force for pore formation. For POPC and DLPC, such hydrophobic-hydrophobic interaction at early stages was facilitated by less alignment of the lipid tails (Fig. 4) as compared to DPPC.

Results for R_g and d_{COM} of the PEI-LA NP followed a similar trend as the PEI NP (Fig. 5e and 5f), where both NP compaction and relaxation from its compacted configurations were observed in all membranes. The relative reduction in R_g was ~5.93%, ~6.62%, and ~5.48%, while the relative reduction in d_{COM} was ~1.55%, ~10.5%, and ~10.04%, respectively for POPC, DPPC and DLPC membranes. This suggests that NP compaction in POPC was mainly attributed to compaction of the PEIs (with little reduction in d_{COM}, Fig. 5e), while compaction in DPPC and DLPC membranes occurred mostly through the reduction in d_{COM}. The minimum R_g was about the same for all membranes, consistent with the similar pore size of the membranes (Fig. S17). For all membranes, the reduction in d_{COM} was much lower for PEI-LA NP than PEI NP, indicating that PEI-LA NP was more rigid than the PEI NP.
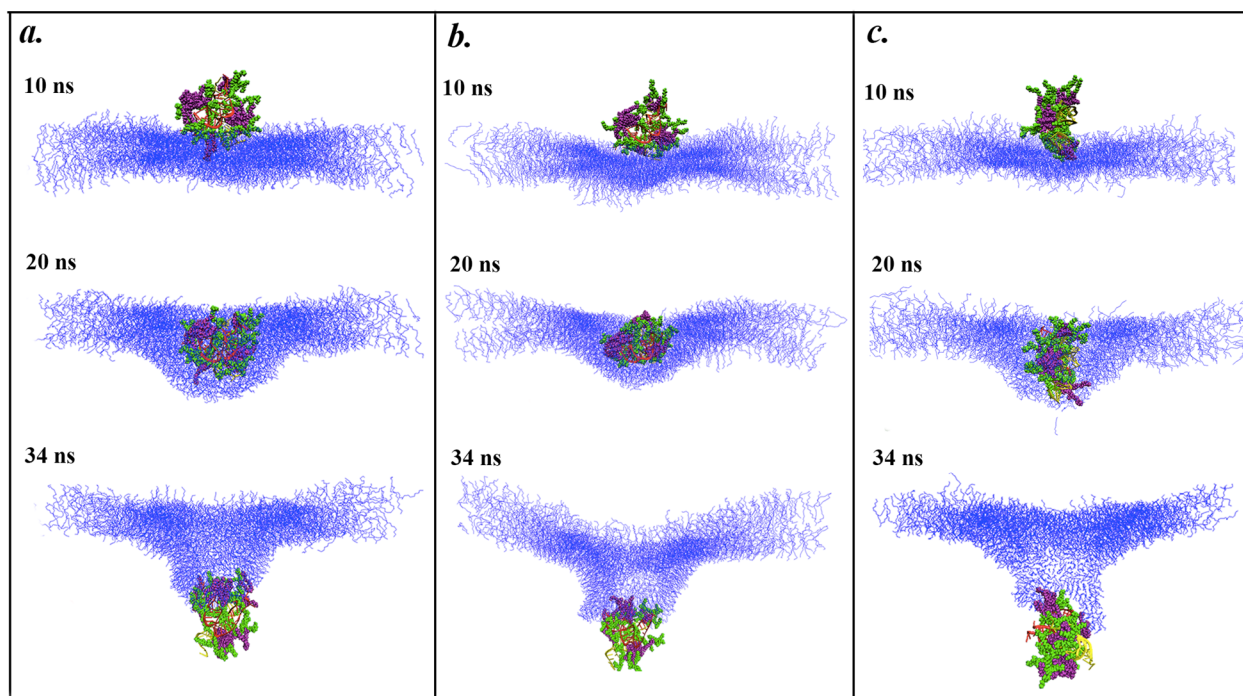

Figure 9. Side-view snapshots of PEI-LA NP crossing (a) POPC, (b) DPPC and (c) DLPC membranes at different time of the SMD simulations. For simplicity of visualization, water, ions, and hydrophilic parts of the membranes were removed and only the hydrophobic acyl chains of the membranes are shown. siRNA molecules are shown in yellow and red. PEI molecules are shown in green, while its hydrophobic LA substitutions are shown in purple.

For the PEI-LA NP, POPC displayed symmetric pore formation while DPPC and DLPC exhibited asymmetric pore formation (Fig. 10a, b, c). As shown earlier, when the PEI NP penetrated the bilayers, the

pore formation was symmetric for DPPC and DLPC, while asymmetric for POPC. Therefore, the type of NP affected the deformation and the extent of disturbance in the membranes. MD simulations for pore resealing (Fig. 10d, e, f) showed that for the same simulation time (64 ns), no full recovery to the flat configuration was observed for the POPC and DLPC membranes. The recovery of DPPC was stronger, but still not as much as what was observed in Fig. 7 for the PEI NP. The number of lipid flip-flops from the bottom leaflet to the top leaflet in each system is shown in Table S3. Lipid flip-flops from the lower leaflet to the upper leaflet occurred for DPPC and DLPC membranes, but not for POPC membrane. Considering that lipid flip-flops did not occur for PEI NP-DPPC system, this shows that LA substitutions facilitated lipid flip-flops in the DPPC. Also, for DLPC, the lipids that underwent flip-flop were spotted at further distance from the initial pore location as compared to DPPC. This was caused by the more asymmetric nature of the pore in DLPC (see SI, section S8) as well as its shorter lipid, which enabled the diffusion of the lipids from the lower leaflet to the upper leaflet to occur earlier in the pore resealing process.
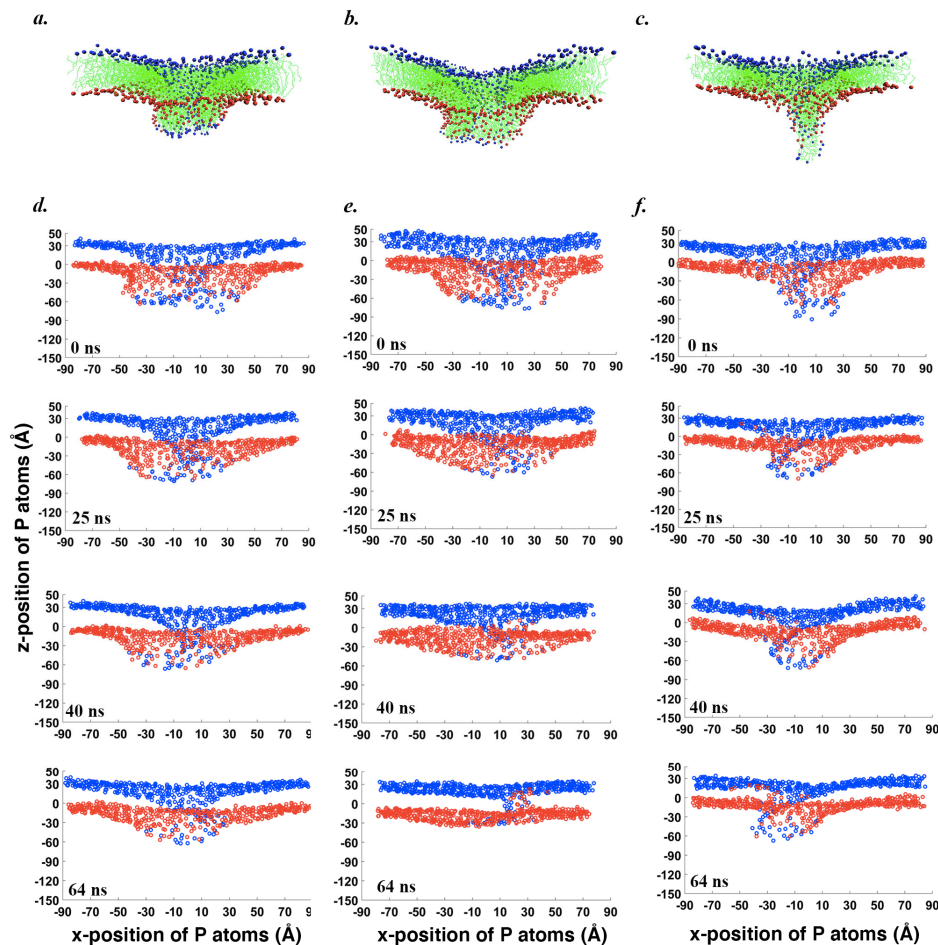
Figure 10. Side view snapshots at 34 ns of the SMD for (a) POPC, (b) DPPC and (c) DLPC membranes with a PEI-LA NP. P atoms of upper and lower leaflets are shown in blue and red, respectively. The lipid tails are shown in green. Positions of P atoms in (d) POPC (e) DPPC and (f) DLPC membranes during pore resealing.

To evaluate the effect of initial NP orientation on the results, 6 additional simulations (3 PEI-LA NP-membrane + 3 pore resealing) were performed. For the PEI-LA NP-membrnane simulations, initial orientation of the NP was chosen such that the axes of its siRNAs were almost parallel to the membrane surface. The simulations results are presented in SI (section S11). For the PEI-LA NP-replica, POPC and DPPC displayed symmetric pore formation while DLPC exhibited asymmetric pore formation (Table S2). The order of symmetry did not change under a different initial orientation and remained as: PEI-LA NP-replica-POPC > PEI-LA NP-replica-DPPC > PEI-LA NP-replica-DLPC. For all three membranes, in-plane distributions of P atoms around the COM of NP (Fig. S18) were similar for the simulations with different

25

initial orientations, where for a well-established pore, two peaks were observed and the pore size was larger for DLPC membrane. Similar to the PEI-LA NP, hydrophobic LA substitutions of PEI-LA NP-replica were exposed to the interiors of the POPC and DLPC membranes while they did not insert themselves into the DPPC bilayer until the very end of the pulling process. Pulling force on the PEI-LA NP-replica displayed similar level of magnitude as the pulling force on PEI-LA NP (Fig. S19), suggesting that membrane resistance against NP entry was not dependent on the initial orientation of NP as it could rotate to minimize membrane disruption. MD simulations for pore resealing (Fig. S20) confirmed the occurrence of lipid flip-flops from the lower leaflet to the upper leaflet for all the replica systems, while the highest number of lipid flip-flops occurred again for the DLPC membrane (Table S3).

DISCUSSION

Implications

During PEI mediated delivery of siRNA, the PEI/siRNA NPs interact with cell membrane that is composed of lipids with different properties [5]. This study investigated membrane response upon interaction with a PEI/siRNA NP using MD and SMD simulations. Three representative zwitterionic membrane models built from POPC, DPPC and DLPC lipids were employed, along with both native and lipid-modified PEI/siRNA NPs. The presence of a double bond on the Sn2 chain of POPC induced a change in the lipid chain's orientation, leading to less alignment between the Sn1 and Sn2 chains. This allowed POPC to have a smaller membrane thickness compared with DPPC, which had similar numbers of Cs on its tails but was completely saturated. The order of membranes can be quantified in both simulations and experiments through the measurement of deuterium order parameter. Several MD simulations and experiments showed that the deuterium order parameters of both Sn1 and Sn2 chains decreased in lipids with unsaturated Cs and the effect was more pronounced in Sn2 chains [7,59]. In addition, among saturated membranes, long-tail lipids had larger deuterium order parameter than short-tail lipids, suggesting that the chains were more aligned in long-tail lipids [60]. Our results are in agreement with these previous reports, where the probability distribution for the angle between Sn1 and Sn2 chains was found to be narrower in

DPPC (long-tail, saturated) than in POPC (long-tail, unsaturated) and DLPC (short-tail, saturated). Our non-equilibrium SMD results also showed that the order of the membranes decreased during NP penetration, resulting in a broader probability distribution and an increase in the most probable angle. This agrees with experiments and previous MD simulations on single polycation interaction with membranes, where polycation was shown to induce disorder of acyl chains in the bilayer organization and reduce packing of the membrane [15].

Less alignment of lipid tails in the bilayer may promote insertion of hydrophobic cationic carriers through hydrophobic interactions, thereby facilitating their entry into the cell. It has been found experimentally that low molecular weight PEI's gene delivery efficacy was improved significantly with the substitution of hydrophobic moieties including aliphatic lipids such as caprylic (8C), myristic (14C), palmitic (16C), stearic (18C), and LA [2,61]. Our group previously observed that gene delivery performance of 2 kDa modified PEI was increased enormously compared to its unmodified counterpart. Here, we found that hydrophobic LA substitutions on the PEI-LA NP were exposed to the interiors of the POPC and DLPC bilayers, while they could not be inserted into the DPPC bilayers. Because of this, the force required for NP penetration was different depending on the types of NP and membrane. Compared with PEI NP, PEI-LA NP required less force to cross the POPC and DLPC membranes, while the force to cross the DPPC membrane was insensitive to the NP type and its initial orientation with respect to the membrane. It has been suggested that hydrophilic polymers with substituted hydrophobic side chains can insert their hydrophobic part into the membrane, and thereby induce pore formation through the "barrel-stove" or "carpet" mechanisms, the latter relying a large change of the membrane's curvature [62,63] . Due to the complexity of polymers in terms of their structure, conformation and phase-separation abilities, it is difficult to predict their exact conformations within a lipid bilayer [62]. However, our results suggest that hydrophobic modifications are more likely to interact with the internal hydrophobic regions of membranes that have less alignment of lipid tails, via a higher content of unsaturated lipids or saturated but short-tail lipids.

Our non-equilibrium SMD simulation trajectories revealed that, as a NP was crossing a membrane, the lipids near the contact zone reoriented themselves to minimize the unfavorable interaction between hydrophilic NP and hydrophobic tails. This caused a hydrophilic pore to be formed in each membrane. *Wikosz et al.*[64] observed that polycation embedded into the POPC membrane led to the reorientation of lipid molecules near the polycation, causing the internalization of several lipid headgroups into the hydrophobic core of the membrane and flux of water into the vicinity of the polycation. Here, depending on the natures of membrane lipid composition as well as type and orientation of NP, we observed two types of pore formations, symmetric and asymmetric. The PEI NP-POPC, PEI-LA NP-DPPC and PEI-LA NP-DLPC systems displayed asymmetric pore formation, while the PEI-LA NP-POPC, PEI NP-DPPC and PEI NP-DLPC systems showed symmetric pore formation. Additionally, the membranes were ranked according to their degree of symmetry as PEI NP-DPPC > PEI-LA NP-POPC > PEI NP-DLPC > PEI NP-POPC > PEI-LA NP-DPPC > PEI-LA NP-DLPC. While a more extensive study is required to determine the exact conditions for the formation of asymmetric vs. symmetric pores, some insight could be drawn from our results. Compared with a symmetric pore, the formation of an asymmetric pore could be associated with certain instability in the membrane during NP penetration. POPC was comparable to DPPC in thickness, however, the unsaturated Cs created misalignment in the lipid tails, increasing the probability of having an instability. Similarly, the short and more dynamic lipid tails in DLPC were also potential source of instability. Interestingly, the presence of hydrophobic LA substitutions changed the pore type from asymmetric to symmetric for POPC, while changing it from symmetric to asymmetric for DLPC and DPPC. It is possible that the easier penetration brought by the interaction of LA with POPC lipids was able to provide extra stabilization for the membrane. On the other hand, the DLPC bilayer was considerably thinner than POPC and easier for the NP to cross. The additional ease brought by the LA substitutions might have made the system too dynamic to be stable. It should be noted that initial orientation of NP affected the formed pore types observed in the membranes. Precise mechanisms behind the interesting observations on pore formation require further investigations.

For both types of NPs and all three membranes, the upper leaflet underwent more profound deformation than the lower leaflet during pore formation. This caused an imbalance in the concentration of lipids in the two leaflets during pore resealing. Additionally, the type of pore formed affected its resealing, where the closure of an asymmetric pore took a longer time than a symmetric pore. During pore resealing and in most of the simulated systems, some lipids from the lower leaflet underwent flip-flops and translocated to the upper leaflet. The degree of lipid flip-flops was higher in asymmetric pores than in symmetric pores with the exception of DLPC systems, where the number of lipid flip-flops was comparable for both pore types (Table S3). Under normal conditions, flip-flop is considered to be an extremely slow process with time scale on the order of seconds, because it requires disruption of the lipid bilayer structure and removal of polar headgroups from the water interface [65]. Experimentally, flip-flops can be measured using chemical probes. *Wimley et al.*[66] measured the rate of lipid flips in DPPC membranes, and suggested the occurrence of flip-flops through transient defects. *Gurtovenko et al.*[67] using MD simulations explored pore mediated flip-flop of membrane lipids. The pore was induced by a transmembrane ion density gradient. The authors proposed the mechanism of flip-flop, where the appearance of a transient pore in the membrane led to diffusive translocation of lipids through the pore. The rate-limiting step in the process of flip-flop was argued to be the formation of water pores [67]. Under equilibrium conditions, pores can be formed but the probability is low due to the significant free energy cost associated with it [68]. *Bennet et al.* [68] using umbrella sampling MD simulations calculated the free energy associated with pore formation across DLPC, DMPC and DPPC bilayers. The reaction coordinate in the umbrellas sampling simulations was the position of the phosphate of a single lipid with respect to the center of mass of the bilayer. The free energy increased as bilayer thickness increased, being ~17, ~45 and ~78 kJ/mol respectively for DLPC, DMPC and DPPC lipid bilayers. *Sapay et al.*[69] using MD simulations measured the potential of mean force (PMF) for moving a single lipid molecule from water to the center of a lipid bilayer. They found the PMF to be 89, 80 and 16 kJ/mol, respectively for POPC, DPPC and DLPC bilayers. Pore formation can be expedited by non-equilibrium conditions, including electroporation, mechanical stress, shock wave, surface active molecules, small cationic peptides, and cationic polymers

[23]. In the present study, pore formation was accelerated through SMD simulations that induced substantial out-of-plane membrane bending and eventually water pore formation, thereby causing the occurrence of flip-flops during a short time span. The simulations of *Sapay et al.*[69] showed that shorter lipids formed pores more easily than longer lipids, and the corresponding pore size was larger. This agrees with our observations where DLPC underwent the most significant lipid flip-flops from the lower leaflet, due to its short and hence more dynamic lipid tails.

Limitations and future perspectives

A more realistic representation of the cell membrane would be a mixture of various lipid species with different distributions at the upper and lower leaflets. Cell membranes are composed of various lipids that display different levels of saturation, chain length, hydrophobicity and surface charges[70]. Glycerophospholipids including phosphatidylcholine (PC), phophatidylethanolamine (PE), phosphatidylserine (PS), phosphatidylinositol (PI), and phosphatidic acid (PA) account for ~70% of the total lipid content of eukaryoric membranes; while the other 30% consists of cholesterol, sphingomyelin (SM), and glycosphingolipids[71]. Additionally, lipid composition can differ considerably between the two leaflets at the cytosolic vs. extracellular interfaces[71]. For example, plasma membrane have an asymmetric lipid distribution, where PC and SM are mainly localized in the extracellular leaflet, whereas PE and PS are exclusively present in the cytoplasmic leaflet [72]. The resulting asymmetry affects the curvature of the membrane, and can impose a transmembrane electrostatic potential difference[70]. In addition to asymmetry in composition, the solvent facing the two leaflets are different in terms of pH, ionic strength, and electric potential[5]. MD simulations that probe such heterogeneous membrane structures and environment will better shed light on the integrity of membranes and the flip-flop process during NP penetration. The effect of lipid flip-flop is expected be more significant in mixed lipid membranes, where the anionic lipids might undergo translocation from the lower leaflet to the upper leaflet. An example of such lipids is PS that is normally located in the inner leaflet of the plasma membrane. If PS undergoes flip-flop from the inner leaflet to the outer leaflet, it can act as an apoptotic signal for lymphocytic cells [73,74].

Therefore, the NP-induced flip-flops might have strong bearing on the fate of cells and might require better understanding in gene delivery efforts.

The MD and SMD simulations employed here provide atomistic level insight, which is unreachable through common experimental tools. However, limitations on the length and time scale of current computing resources do not allow us to investigate the full-scale dynamics of complex biological systems. For example, the size of our simulated NPs is ~3 nm, while the size of polymeric NPs for nucleic acid delivery is reported to be in the 100-200 nm range [32].The relaxation of lipidic membranes might take longer than our simulation time [75]. Additionally, current all-atom simulations only permit simulations of systems involving $<10^6$ atoms for less than one μs, which is much smaller than those under real experimental conditions[1]. Because of this, direct quantitative comparisons cannot be made between the simulation results and the experimental observations. One approach to model more realistic simulation systems is using coarse grained (CG) methods such as dissipative particle dynamics. However, CG approaches cause a loss of atomistic information of the simulated systems especially in terms of subtle difference between lipid species. Here, using simplified model bilayers, we were able to provide insights into how delicate differences, in terms of length of lipid acyl chains and saturation levels, between different lipids of cell membranes affect membrane response upon interaction with NPs. Our observation of insertion of LA substitution into hydrophobic part of the membranes with less aligned lipid tails is intriguing and of high interest to the design of better siRNA carriers.

The SMD simulations reported here are non-equilibrium simulations that might not exactly represent trajectories that could occur in the absence of an external force. However, comparison among different systems under the same pulling speed has allowed us to assess the NP and membrane deformations and how they are affected by the nature of the membrane lipids, while minimizing the computational cost [39]. The SMD simulations not only accelerated the penetration process, which is difficult to observe for large and complex NP under MD simulations, but also mimicked the situation where the NP is pulled by external forces towards the interior of the cell membrane[76]. Such methodology was previously validated against

experiments on the ability of membrane lipids to dissociate PEI/siRNA NPs[24], as well as on the stability of the NPs during membrane crossing enhanced by LA substitutions [24].

CONCLUSIONS

Membrane deformation, pore formation and resealing during the penetration of PEI and PEI-LA NPs were studied by a series of SMD and MD simulations. Three membrane models based on POPC, DPPC and DLPC lipids were utilized. We found that acyl chains of POPC and DLPC were less aligned than DPPC. Long-tailed LA substitutions could insert themselves into hydrophobic part of the membranes with less aligned tails, thereby reducing the force for NP penetration. Depending on the nature of NPs and membrane models, different types of pores were formed. During pore resealing, membrane lipids were observed to undergo different levels of pore-mediated flip-flops. POPC and DPPC membranes showed lower level of lipid flip-flops due to their long acyl chains, while DLPC membrane showed the largest number of lipid flip-flops due to its short and highly dynamic acyl chains. These mechanistic observations provide valuable insight into membranes deformation and pore evolution caused by the PEI/siRNA NPs, and could facilitate the design of more efficient gene delivery systems.

Conflicts of interest

There are no conflicts to declare.

References

[1]   D. Meneksedag-Erol, T. Tang, H. Uludağ, Molecular modeling of polynucleotide complexes, Biomaterials. 35 (2014) 7068–7076. https://doi.org/10.1016/j.biomaterials.2014.04.103.

[2]   D. Meneksedag-Erol, R.B. KC, T. Tang, H. Uludağ, A Delicate Balance When Substituting a Small Hydrophobe onto Low Molecular Weight Polyethylenimine to Improve Its Nucleic Acid Delivery Efficiency, ACS Appl. Mater. Interfaces. 7 (2015) 24822–24832. https://doi.org/10.1021/acsami.5b07929.

[3]   H.M. Aliabadi, R.B. KC, E. Bousoik, R. Hall, A. Barbarino, B. Thapa, M. Coyle, P. Mahdipoor, H. Uludağ, A systematic comparison of lipopolymers for siRNA delivery to multiple breast cancer cell lines: In vitro studies, Acta Biomater. 102 (2020) 351–366.

[4]   D. Meneksedag-Erol, T. Tang, H. Uludağ, Mechanistic insights into the role of glycosaminoglycans in delivery of polymeric nucleic acid nanoparticles by molecular dynamics simulations, Biomaterials. 156 (2018) 107–120. https://doi.org/10.1016/j.biomaterials.2017.11.037.

[5]   S.J. Marrink, V. Corradi, P.C.T. Souza, H.I. Ingólfsson, D.P. Tieleman, M.S.P. Sansom, Computational Modeling of Realistic Cell Membranes, Chem. Rev. 119 (2019) 6184–6226. https://doi.org/10.1021/acs.chemrev.8b00460.

[6]   P.A. Janmey, P.K.J. Kinnunen, Biophysical properties of lipids and dynamic membranes, Trends Cell Biol. 16 (2006) 538–546.

[7]   M.T. Hyvönen, P.T. Kovanen, Molecular dynamics simulations of unsaturated lipid bilayers: effects of varying the numbers of double bonds, Eur. Biophys. J. 34 (2005) 294–305. https://doi.org/10.1007/s00249-004-0455-7.

[8]   Z. Xu, L. Gao, P. Chen, L.-T. Yan, Diffusive transport of nanoscale objects through cell membranes: a computational perspective, Soft Matter. 16 (2020) 3869–3881.

[9]   Z. Shen, W. Baker, H. Ye, Y. Li, pH-Dependent aggregation and pH-independent cell membrane adhesion of monolayer-protected mixed charged gold nanoparticles, Nanoscale. 11 (2019) 7371–7385.

[10]   P. Chen, H. Yue, X. Zhai, Z. Huang, G.-H. Ma, W. Wei, L.-T. Yan, Transport of a graphene nanosheet sandwiched inside cell membranes, Sci. Adv. 5 (2019) eaaw3192.

[11]   L. Zhang, Z. Zhang, M. Negahban, A. Jérusalem, Molecular dynamics simulation of cell membrane pore sealing, Extrem. Mech. Lett. 27 (2019) 83–93. https://doi.org/10.1016/j.eml.2019.01.008.

[12]   H. Leontiadou, A.E. Mark, S.J. Marrink, Molecular Dynamics Simulations of Hydrophilic Pores in Lipid Bilayers, Biophys. J. 86 (2004) 2156–2164. https://doi.org/10.1016/S0006-3495(04)74275-7.

[13]   U. Kwolek, D. Jamr??z, M. Janiczek, M. Nowakowska, P. Wydro, M. Kepczynski, Interactions of Polyethylenimines with Zwitterionic and Anionic Lipid Membranes, Langmuir. 32 (2016) 5004–5018. https://doi.org/10.1021/acs.langmuir.6b00490.

[14]   C. Zhang, F.-G. Wu, P. Hu, Z. Chen, Interaction of polyethylenimine with model cell membranes studied by linear and nonlinear spectroscopic techniques, J. Phys. Chem. C. 118 (2014) 12195–12205.

[15]   N. Awasthi, W. Kopec, N. Wilkosz, D. Jamróz, J.S. Hub, M. Zatorska, R. Petka, M. Nowakowska, M. Kepczynski, Molecular Mechanism of Polycation-Induced Pore Formation in Biomembranes, ACS Biomater. Sci. Eng. 5 (2019) 780–794. https://doi.org/10.1021/acsbiomaterials.8b01495.

[16]   D.P. Tieleman, The molecular basis of electroporation, BMC Biochem. 5 (2004) 10.

[17]   A.A. Gurtovenko, A.S. Lyulina, Electroporation of asymmetric phospholipid membranes, J. Phys. Chem. B. 118 (2014) 9909–9918.

[18]   R. Reigada, Electroporation of heterogeneous lipid membranes, Biochim. Biophys. Acta (BBA)-Biomembranes. 1838 (2014) 814–821.

[19]   S.A. Kirsch, R.A. Böckmann, Membrane pore formation in atomistic and coarse-grained

simulations, Biochim. Biophys. Acta (BBA)-Biomembranes. 1858 (2016) 2266–2277.

[20] M.L. Fernández, G. Marshall, F. Sagués, R. Reigada, Structural and kinetic molecular dynamics study of electroporation in cholesterol-containing bilayers, J. Phys. Chem. B. 114 (2010) 6855–6865.

[21] M.J. Ziegler, P.T. Vernier, Interface water dynamics and porating electric fields for phospholipid bilayers, J. Phys. Chem. B. 112 (2008) 13588–13596.

[22] X. Zhuang, E.M. Dávila-Contreras, A.H. Beaven, W. Im, J.B. Klauda, An extensive simulation study of lipid bilayer properties with different head groups, acyl chain lengths, and chain saturations, Biochim. Biophys. Acta - Biomembr. 1858 (2016) 3093–3104. https://doi.org/10.1016/j.bbamem.2016.09.016.

[23] Y. Nademi, T. Tang, H. Uludağ, Steered molecular dynamics simulations reveal a self-protecting configuration of nanoparticles during membrane penetration, Nanoscale. 10 (2018) 17671–17682. https://doi.org/10.1039/C8NR04287J.

[24] Y. Nademi, T. Tang, H. Uludağ, Membrane lipids destabilize short interfering ribonucleic acid (siRNA)/polyethylenimine nanoparticles, Nanoscale. 12 (2020) 1032–1045. https://doi.org/10.1039/C9NR08128C.

[25] H.M. Aliabadi, B. Landry, P. Mahdipoor, C.Y.M. Hsu, H. Uludağ, Effective down-regulation of Breast Cancer Resistance Protein (BCRP) by siRNA delivery using lipid-substituted aliphatic polymers, Eur. J. Pharm. Biopharm. 81 (2012) 33–42. https://doi.org/10.1016/j.ejpb.2012.01.011.

[26] H. Montazeri Aliabadi, B. Landry, P. Mahdipoor, H. Uludağ, Induction of Apoptosis by Survivin Silencing through siRNA Delivery in a Human Breast Cancer Cell Line, Mol. Pharm. 8 (2011) 1821–1830. https://doi.org/10.1021/mp200176v.

[27] M. Abbasi, H.M. Aliabadi, E.H. Moase, A. Lavasanifar, K. Kaur, R. Lai, C. Doillon, H. Uludağ, siRNA-Mediated Down-Regulation of P-glycoprotein in a Xenograft Tumor Model in NOD-SCID Mice, Pharm. Res. 28 (2011) 2516–2529. https://doi.org/10.1007/s11095-011-0480-z.

[28] K. Utsuno, H. Uludağ, Thermodynamics of Polyethylenimine-DNA Binding and DNA Condensation, Biophys. J. 99 (2010) 201–207. https://doi.org/10.1016/j.bpj.2010.04.016.

[29] J. Suh, H. Paik, B.K. HwANG, Ionization of Poly (ethylenimine) and Poly (allylamine) at Various pH′ s, Bioorg. Chem. 22 (1994) 318–327.

[30] J. Nagaya, M. Homma, A. Tanioka, A. Minakata, Relationship between protonation and ion condensation for branched poly (ethylenimine), Biophys. Chem. 60 (1996) 45–51.

[31] G.J.M. Koper, R.C. van Duijvenbode, D.D.P.W. Stam, U. Steuerle, M. Borkovec, Synthesis and protonation behavior of comblike poly (ethyleneimine), Macromolecules. 36 (2003) 2500–2507.

[32] H.M. Aliabadi, B. Landry, C. Sun, T. Tang, H. Uludağ, Supramolecular assemblies in functional siRNA delivery: where do we stand?, Biomaterials. 33 (2012) 2546–2569.

[33] W.L. Jorgensen, Quantum and statistical mechanical studies of liquids. 10. Transferable intermolecular potential functions for water, alcohols, and ethers. Application to liquid water, J. Am. Chem. Soc. 103 (1981) 335–340. https://doi.org/10.1021/ja00392a016.

[34] E.L. Wu, X. Cheng, S. Jo, H. Rui, K.C. Song, E.M. Dávila-Contreras, Y. Qi, J. Lee, V. Monje-Galvan, R.M. Venable, CHARMM-GUI membrane builder toward realistic biological membrane simulations, J. Comput. Chem. 35 (2014) 1997–2004.

[35] B.R. Brooks, C.L. Brooks III, A.D. Mackerell Jr, L. Nilsson, R.J. Petrella, B. Roux, Y. Won, G. Archontis, C. Bartels, S. Boresch, CHARMM: the biomolecular simulation program, J. Comput. Chem. 30 (2009) 1545–1614.

[36] S. Jo, T. Kim, V.G. Iyer, W. Im, CHARMM-GUI: a web-based graphical user interface for CHARMM, J. Comput. Chem. 29 (2008) 1859–1865.

[37] N. Kučerka, Y. Liu, N. Chu, H.I. Petrache, S. Tristram-Nagle, J.F. Nagle, Structure of Fully Hydrated Fluid Phase DMPC and DLPC Lipid Bilayers Using X-Ray Scattering from Oriented Multilamellar Arrays and from Unilamellar Vesicles, Biophys. J. 88 (2005) 2626–2637. https://doi.org/10.1529/biophysj.104.056606.

[38] J. Lee, X. Cheng, J.M. Swails, M.S. Yeom, P.K. Eastman, J.A. Lemkul, S. Wei, J. Buckner, J.C.

Jeong, Y. Qi, CHARMM-GUI input generator for NAMD, GROMACS, AMBER, OpenMM, and CHARMM/OpenMM simulations using the CHARMM36 additive force field, J. Chem. Theory Comput. 12 (2015) 405–413.

[39]   S. Park, F. Khalili-Araghi, E. Tajkhorshid, K. Schulten, Free energy calculation from steered molecular dynamics simulations using Jarzynski's equality, J. Chem. Phys. 119 (2003) 3559–3566. https://doi.org/10.1063/1.1590311.

[40]   Q. Wei, W. Zhao, Y. Yang, B. Cui, Z. Xu, X. Yang, Method Evaluations for Adsorption Free Energy Calculations at the Solid/Water Interface through Metadynamics, Umbrella Sampling, and Jarzynski's Equality, ChemPhysChem. 210009 (2018) 1–14. https://doi.org/10.1002/cphc.201701241.

[41]   H. Nguyen, N. Do, T. Phan, T. Pham, Steered Molecular Dynamics for Investigating the Interactions Between Insulin Receptor Tyrosine Kinase (IRK) and Variants of Protein Tyrosine Phosphatase 1B (PTP1B), Appl. Biochem. Biotechnol. 184 (2018) 401–413. https://doi.org/10.1007/s12010-017-2549-6.

[42]   Y. Xu, J. Shen, X. Luo, I. Silman, J.L. Sussman, K. Chen, H. Jiang, How does huperzine A enter and leave the binding gorge of acetylcholinesterase? Steered molecular dynamics simulations, J. Am. Chem. Soc. 125 (2003) 11340–11349.

[43]   D.J. Brockwell, E. Paci, R.C. Zinober, G.S. Beddard, P.D. Olmsted, D.A. Smith, R.N. Perham, S.E. Radford, Pulling geometry defines the mechanical resistance of a β-sheet protein, Nat. Struct. Mol. Biol. 10 (2003) 731.

[44]   S. Azadi, M. Tafazzoli-Shadpour, R. Omidvar, Steered Molecular Dynamics Simulation Study of Quantified Effects of Point Mutation Induced by Breast Cancer on Mechanical Behavior of E-Cadherin, Mol. Biol. 52 (2018) 723–731.

[45]   H. Lu, K. Schulten, Steered molecular dynamics simulations of force-induced protein domain unfolding, Proteins Struct. Funct. Bioinforma. 35 (1999) 453–463.

[46]   C. Sun, T. Tang, H. Uludag, A molecular dynamics simulation study on the effect of lipid substitution on polyethylenimine mediated siRNA complexation, Biomaterials. 34 (2013) 2822–2833. https://doi.org/10.1016/j.biomaterials.2013.01.011.

[47]   E.J. Denning, U.D. Priyakumar, L. Nilsson, A.D. Mackerell, Impact of 2′-hydroxyl sampling on the conformational properties of RNA: Update of the CHARMM all-atom additive force field for RNA, J. Comput. Chem. 32 (2011) 1929–1943. https://doi.org/10.1002/jcc.21777.

[48]   J.B. Klauda, R.M. Venable, J.A. Freites, J.W. O'Connor, D.J. Tobias, C. Mondragon-Ramirez, I. Vorobyov, A.D. MacKerell, R.W. Pastor, A.D. MacKerell Jr, R.W. Pastor, Update of the CHARMM all-atom additive force field for lipids: validation on six lipid types, J. Phys. Chem. B. 114 (2010) 7830–7843. https://doi.org/10.1021/jp101759q.

[49]   J.C. Phillips, R. Braun, W. Wang, J. Gumbart, E. Tajkhorshid, E. Villa, C. Chipot, R.D. Skeel, L. Kalé, K. Schulten, Scalable molecular dynamics with NAMD, J. Comput. Chem. 26 (2005) 1781–1802. https://doi.org/10.1002/jcc.20289.

[50]   T. Darden, D. York, L. Pedersen, Particle mesh Ewald: An $N \cdot \log(N)$ method for Ewald sums in large systems, J. Chem. Phys. 98 (1993) 10089–10092. https://doi.org/10.1063/1.464397.

[51]   J.-P. Ryckaert, G. Ciccotti, H.J.. Berendsen, Numerical integration of the cartesian equations of motion of a system with constraints: molecular dynamics of n-alkanes, J. Comput. Phys. 23 (1977) 327–341. https://doi.org/10.1016/0021-9991(77)90098-5.

[52]   G.J. Martyna, D.J. Tobias, M.L. Klein, Constant pressure molecular dynamics algorithms, J. Chem. Phys. 101 (1994) 4177–4189.

[53]   S.E. Feller, Y. Zhang, R.W. Pastor, B.R. Brooks, Constant pressure molecular dynamics simulation: the Langevin piston method, J. Chem. Phys. 103 (1995) 4613–4621.

[54]   W. Humphrey, A. Dalke, K. Schulten, VMD: Visual molecular dynamics, J. Mol. Graph. 14 (1996) 33–38. https://doi.org/10.1016/0263-7855(96)00018-5.

[55]   S. Garcia-Manyes, L. Redondo-Morata, G. Oncins, F. Sanz, Nanomechanics of Lipid Bilayers: Heads or Tails?, J. Am. Chem. Soc. 132 (2010) 12874–12886. https://doi.org/10.1021/ja1002185.

[56]   D. Bochicchio, L. Monticelli, The Membrane Bending Modulus in Experiments and Simulations: A Puzzling Picture, in: Adv. Biomembr. Lipid Self-Assembly, 1st ed., Elsevier Inc., 2016: pp. 117–143. https://doi.org/10.1016/bs.abl.2016.01.003.

[57]   J.F. Nagle, Experimentally determined tilt and bending moduli of single-component lipid bilayers, Chem. Phys. Lipids. 205 (2017) 18–24. https://doi.org/10.1016/j.chemphyslip.2017.04.006.

[58]   M. Doktorova, D. Harries, G. Khelashvili, Determination of bending rigidity and tilt modulus of lipid membranes from real-space fluctuation analysis of molecular dynamics simulations, Phys. Chem. Chem. Phys. 19 (2017) 16806–16818.

[59]   L.L. Holte, S.A. Peter, T.M. Sinnwell, K. Gawrisch, 2H nuclear magnetic resonance order parameter profiles suggest a change of molecular shape for phosphatidylcholines containing a polyunsaturated acyl chain, Biophys. J. 68 (1995) 2396–2403.

[60]   J.P.M. Jämbeck, A.P. Lyubartsev, Derivation and systematic validation of a refined all-atom force field for phosphatidylcholine lipids, J. Phys. Chem. B. 116 (2012) 3164–3179.

[61]   A. Neamnark, O. Suwantong, R.B. K. C., C.Y.M. Hsu, P. Supaphol, H. Uludağ, Aliphatic Lipid Substitution on 2 kDa Polyethylenimine Improves Plasmid Delivery and Transgene Expression, Mol. Pharm. 6 (2009) 1798–1815. https://doi.org/10.1021/mp900074d.

[62]   W.H. Binder, Polymer-Induced Transient Pores in Lipid Membranes, Angew. Chemie Int. Ed. 47 (2008) 3092–3095.

[63]   Y. Shai, Mechanism of the binding, insertion and destabilization of phospholipid bilayer membranes by α-helical antimicrobial and cell non-selective membrane-lytic peptides, Biochim. Biophys. Acta (BBA)-Biomembranes. 1462 (1999) 55–70.

[64]   N. Wilkosz, D. Jamróz, W. Kopeć, K. Nakai, S. Yusa, M. Wytrwal-Sarna, J. Bednar, M. Nowakowska, M. Kepczynski, Effect of polycation structure on interaction with lipid membranes, J. Phys. Chem. B. 121 (2017) 7318–7326.

[65]   F.Y. Jiang, Y. Bouret, J.T. Kindt, Molecular Dynamics Simulations of the Lipid Bilayer Edge, Biophys. J. 87 (2004) 182–192. https://doi.org/10.1529/biophysj.103.031054.

[66]   W.C. Wimley, T.E. Thompson, Transbilayer and interbilayer phospholipid exchange in dimyristoylphosphatidylcholine/dimyristoylphosphatidylethanolamine large unilamellar vesicles, Biochemistry. 30 (1991) 1702–1709.

[67]   A.A. Gurtovenko, I. Vattulainen, Molecular mechanism for lipid flip-flops, J. Phys. Chem. B. 111 (2007) 13554–13559.

[68]   W.F.D. Bennett, N. Sapay, D.P. Tieleman, Atomistic Simulations of Pore Formation and Closure in Lipid Bilayers, Biophys. J. 106 (2014) 210–219. https://doi.org/10.1016/j.bpj.2013.11.4486.

[69]   N. Sapay, W.F.D. Bennett, D.P. Tieleman, Thermodynamics of flip-flop and desorption for a systematic series of phosphatidylcholine lipids, Soft Matter. 5 (2009) 3295. https://doi.org/10.1039/b902376c.

[70]   G. Van Meer, D.R. Voelker, G.W. Feigenson, Membrane lipids: Where they are and how they behave, Nat. Rev. Mol. Cell Biol. 9 (2008) 112–124. https://doi.org/10.1038/nrm2330.

[71]   P.A. Leventis, S. Grinstein, The Distribution and Function of Phosphatidylserine in Cellular Membranes, Annu. Rev. Biophys. 39 (2010) 407–427. https://doi.org/10.1146/annurev.biophys.093008.131234.

[72]   F.-X. Contreras, L. Sánchez-Magraner, A. Alonso, F.M. Goñi, Transbilayer (flip-flop) lipid motion and lipid scrambling in membranes, FEBS Lett. 584 (2010) 1779–1786. https://doi.org/10.1016/j.febslet.2009.12.049.

[73]   R.A. Schlegel, P. Williamson, Phosphatidylserine, a death knell, Cell Death Differ. 8 (2001) 551–563.

[74]   J. Razzokov, M. Yusupov, S. Vanuytsel, E.C. Neyts, A. Bogaerts, Phosphatidylserine flip-flop induced by oxidation of the plasma membrane: a better insight by atomic scale modeling, Plasma Process. Polym. 14 (2017) 1–6. https://doi.org/10.1002/ppap.201700013.

[75]   C. Neale, W.F.D. Bennett, D.P. Tieleman, R. Pomes, Statistical convergence of equilibrium properties in simulations of molecular solutes embedded in lipid bilayers, J. Chem. Theory

Comput. 7 (2011) 4175–4188.

[76] A.A. Gurtovenko, J. Anwar, I. Vattulainen, Defect-mediated trafficking across cell membranes: insights from in silico modeling, Chem. Rev. 110 (2010) 6077–6103.